ARTICLE

OPEN

Modifying graphene's lattice dynamics by hot-electron injection from single gold nanoparticles

Marcel Weinhold[1], Sangam Chatterjee[1] & Peter J. Klar[1]

Two-dimensional layered materials like graphene pave the way to advanced (opto-) electronic devices. Their extraordinary properties can be further controlled employing plasmonic nanostructures. The interplay between two-dimensional material and plasmonic nanostructures yields enhanced light focusing, large absorption cross sections, and hot-carrier generation due to the excitation and decay of localized surface plasmons. However, this interplay strongly depends on the particle's environment and geometry mandating the investigation of individual structures. Here, we show that Raman spectroscopy reveals locally resolved information about charge transfer, temperature, and strain distribution of graphene sheets in the vicinity of individual spherical gold nanoparticles. Hot-electrons are efficiently injected into graphene under resonant excitation of the localized surface plasmons of the gold nanoparticle. Additionally, heating of the graphene sheet and its intrinsic strain can be separated and quantified. Hence, the presented analysis provides unprecedented insights into the underlying microscopic physics enabling better device design in the future.

[1] Institute of Experimental Physics I and Center for Materials Research, Justus Liebig University Giessen, Heinrich-Buff-Ring 16, 35392 Giessen, Germany. Correspondence and requests for materials should be addressed to P.J.K. (email: peter.j.klar@physik.uni-giessen.de)

Graphene, the two-dimensional manifestation of sp^2-hybridized carbon atoms arranged in a honeycomb structure, was first experimentally verified by Novoselov and Geim in 2004[1]. Since then, it has been studied intensively resulting in the revelation of numerous extraordinary properties[2–6]. Consequently, graphene is discussed as material for a variety of applications including thermal management, membrane technology, and next-generation (opto-) electronic devices[7–12]. Hence, the role of contacts, carrier injection, and compatibility with conventional, metal-based electronics are of utmost importance requiring in-depth studies of nanostructured devices.

Nanoscale metal contacts display plasmonic properties, which can drastically alter their electrical properties as well as their optical response. Hence, hybrids combining graphene and plasmonic nanostructures may not only serve as model systems for contacts in carrier injection or carrier extraction experiments but also feature an enhanced optical-absorption cross-section compared to pristine graphene[13]. Well-designed plasmonic structures lead to a near-field confinement of the incident light due to the excitation of collective free-carrier oscillations, so-called localized surface plasmons (LSP)[14–16]. Such LSPs cause enormous electric-field enhancements. The excitation of LSPs is a resonant process and the resonance energy is a function of the optical properties of the structure's material and the surrounding medium. Hence, the resonance frequency may lie within the visible or near-infrared region of the electromagnetic spectrum depending on the size and the shape of the plasmonic structure. Excited LSPs may decay into energy-rich electron-hole pairs due to Landau damping[17]. Such 'hot-carriers' have recently received significant attention across many disciplines as they, e.g., enable successful photocatalysis[18,19] or photothermal desalination[20,21]. In graphene-based devices, hot-carriers may generate photo-currents[22] or locally increase the electron density leading, for example, to the formation of pn-junctions[23].

The use of gold as material for plasmonic nanostructures in such devices is preferable for various reasons[24–26]. Desirable features include the low contact barrier between gold and graphene of approx. 0.6 eV[27,28]. Furthermore, the dielectric characteristics typically yield plasmonic resonances in the visible or near-infrared range of the electromagnetic spectrum, and the chemical inertness of gold at ambient conditions guarantees longevity of the hybrid arrangement.

Intuitively, the electronic properties will dominate the effects of hot-carrier injection[29]. However, the strong electron–phonon coupling in graphene also should yield an influence of the free-carrier concentration on graphene's phonon dispersion relation. This is theoretically described either by plasmon–phonon coupling[20,30] or by dynamic electron–phonon coupling[31,32]. So far, only little experimental evidence supports these fundamental claims[33–35]. Currently, a unified theory does not exist, as yet existing theories do not even conclusively agree.

In this work, we reveal the intricate interplay between hot-electrons injected from plasmonic nanoparticles into graphene and graphene's phonons and show how the coupling between them alters quantifiably graphene's phonon dispersion relation. Spatially resolved micro-Raman spectroscopy is an ideally suited tool for this study as the generation of hot-electrons due to the excitation laser and the detection of the corresponding Raman spectra occur simultaneously and on the same spot. Furthermore, micro-Raman spectroscopy provides an easy access to single particle measurements, which is desirable since the plasmonic properties of such particles vary drastically with the particle's size and shape. We study individual nanoparticles positioned on single-layer graphene on quartz substrates by Raman microscopy. The nanospheres consist either of pristine gold or of silica-shelled gold. In particular, we perform Raman mappings on such individual nanoparticles employing different excitation wavelengths in order to realize excitation conditions on-resonance and off-resonance with the nanoparticle's LSPs.

Results

Raman mappings in the vicinity of a gold nanoparticle. The top curve in Fig. 1a displays a characteristic Stokes Raman spectrum of graphene. The graphene structure belongs to the space group $P6/mmm$ according to Hermann-Mauguin notation[36]. The so-called G mode is associated with sp^2-hybridized carbon where the sublattices of the two inequivalent carbon atoms per unit cell vibrate against each other[37,38]. It is the only mode in graphene's Raman spectrum originating from an ordinary first-order phonon Raman process. It corresponds to the excitation of the degenerate transverse optical (TO) phonons and the longitudinal optical (LO) phonons with E_{2g} symmetry at the Γ-point of the 1st Brillouin zone[38]. Both, the so-called D mode and the 2D mode (sometimes referred-to as G′ mode) involve the excitation of TO phonons with A_{1g} symmetry near the K or K′ points[36]. Defect scattering in case of the D mode and the simultaneous excitation of two phonons with momenta of equal magnitude in case of the 2D mode ensure the conservation of momentum. Consequently, the D mode is a defect-induced mode while the 2D mode is a two-phonon Raman process and does not require the presence of defects. All three modes show characteristic changes in the presence of gold nanoparticles (see Fig. 1b) as shown in the lower set of spectra in Fig. 1a. Here, the spot is scanned across the gold nanoparticle as indicated by the pictograms. The spectra are normalized to the intensity of the 2D mode and the corresponding factors denote the normalization factors of the 2D mode. The nanoparticle strongly enhances the three Raman signals in its vicinity. Two major effects related to the transceiver action of gold nanoparticles cause the enhancement: receiver action is due to the formation of LSPs. The confinement of the incident light leads to a significant increase in the squared electric-field strength that, in turn, is proportional to the scattered Raman intensity. Emitter action is due to a coupling of the near-field Raman-scattered light to the far-field by the metallic nanoparticle that effectively acts as an antenna. The presence of the strong Raman enhancement indicates a rather resonant LSP excitation. Furthermore, gold nanoparticles act as local defects. This is corroborated by the ratio between the signals of the defect-induced D mode and the G mode of graphene that increases from a value of nearly 0.3 to more than a value of 1 at the particle site while the intensity ratio between 2D and G mode is almost constant (see Fig. 1a).

Corresponding spatial mappings of the Raman intensity of graphene in the vicinity of a pristine gold nanoparticle obtained using an excitation wavelength of 633 nm are shown in false colors for the D, the G, and the 2D Raman modes, from top to bottom in Fig. 1c, respectively. The dashed horizontal lines indicate the positions where the spectra plotted in panel a were recorded. The spatial extent of the enhancement appears to be larger than the actual particle size since these maps originate from a convolution of the actual particle size and the virtually diffraction-limited laser spot. The nanoparticle not only enhances the intensities of the Raman signals, but also influences their Raman shifts. The Raman shifts correspond to the vibrational frequencies of the excited optical phonon branch at specific wave vectors, that is, at characteristic points of the 1st Brillouin zone (the G mode corresponds to the Γ-point, the 2D mode to the K and the K′-points). Hence, they offer direct access to specific points of the phonon dispersion relation, which is very sensitive to strain, temperature, and coupling of the phonons with other excitations.

In the following, we will focus on the 2D mode and the G mode Raman signals as the underlying microscopic processes are solely determined by the intrinsic phonons of graphene and do not
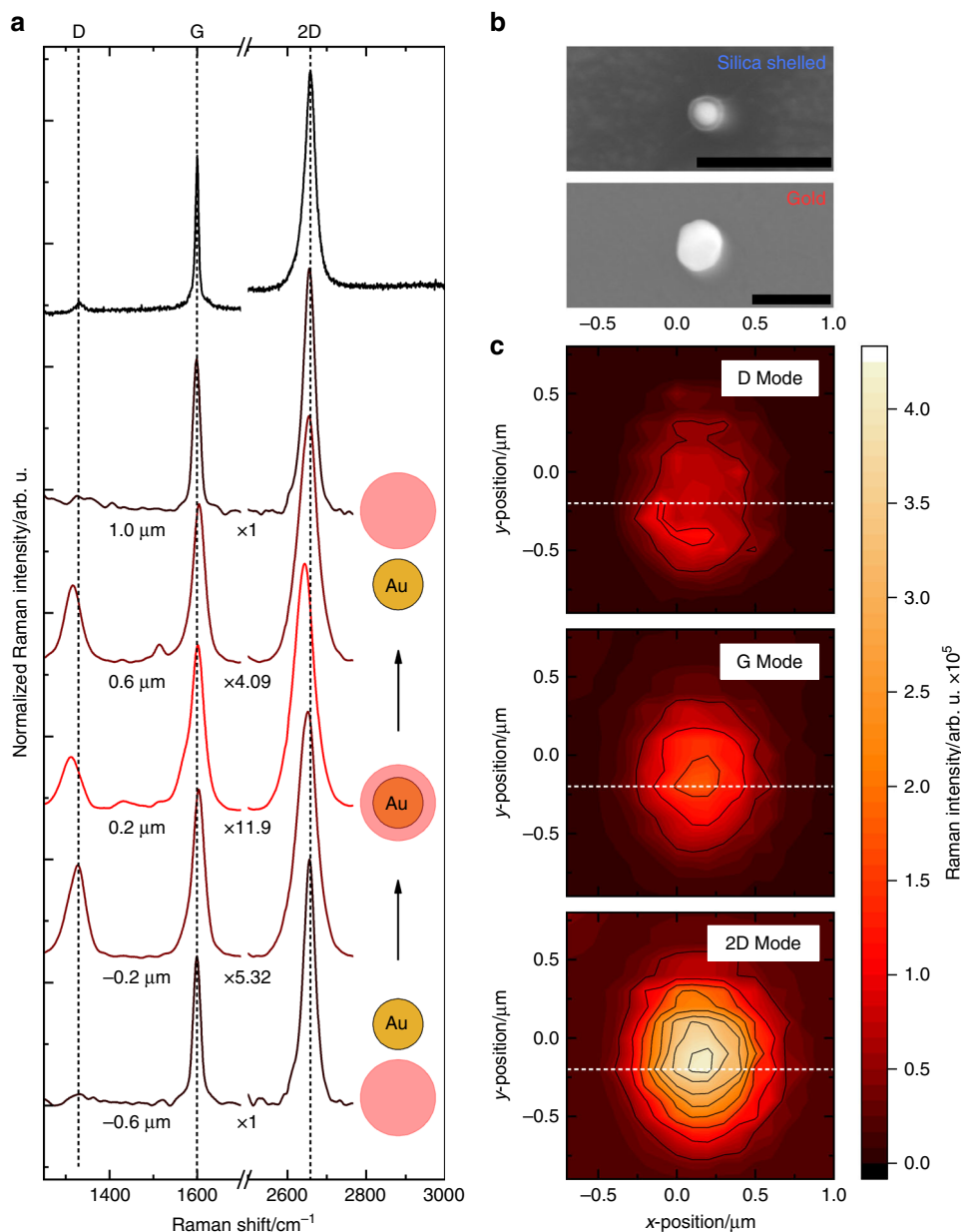
Fig. 1 Intensity of the Raman signal in the vicinity of a gold nanoparticle. **a** Series of Raman spectra of graphene obtained by scanning along the line indicated in the three images (**c**) that contains the position of strongest enhancement. The laser wavelength of 633 nm is in-resonance with the localized surface plasmon absorption of the gold nanoparticle. The top spectrum has been taken on a pristine graphene sample. The positions of Raman modes D, G, and 2D of pristine graphene are indicated by dashed vertical lines. All spectra are normalized to the intensity of the 2D mode, the corresponding normalization factors are given in the figure. The dashed vertical lines indicate the frequencies of the unperturbed Raman modes, i.e., not affected by the presence of the nanoparticle. **b** Scanning electron microscopy images of typical silica-shelled gold nanoparticle and pristine gold nanoparticle used in this study. Each scale bar corresponds to a length of 500 nm. The gold particles appear rather bright, while the silica shell in case of the lower image appears as a halo surrounding the brighter inner sphere associated with the gold nanoparticle. **c** Intensity maps of the three Raman modes around an individual gold nanoparticle

involve defects. Note that this restriction does not imply a loss of information as both, the D mode and the 2D mode involve the excitation of optical phonons near the K and the K' points.

Hot-electron injection and plasmon–phonon coupling. Figure 2a and b depict the spatial maps of the Raman shifts of the G mode and the 2D mode corresponding to the intensity maps shown in Fig. 1. Both, the G mode representative for wave vectors $|\mathbf{q}| \approx 0$ close to the Γ-point and the 2D mode that is representative for phonons of larger $|\mathbf{q}|$ close to the K and the K'-points exhibit a distinct dependence of the mode frequency on spatial position,

which correlates systematically with the particle position. Intriguingly, the modes do not shift in the same manner, which is even better visible in the comparison of the corresponding Raman shift profiles (Fig. 2c). The 2D mode undergoes a red-shift when approaching the nanoparticle, whereas the G mode exhibits a blue-shift. This behavior can consistently be explained by a quantum-mechanical level anti-crossing between the phonon modes and free-carrier excitations. The phonon-like mode shifts upwards in frequency at the Γ-point and downwards in frequency close to the K and K' points of the 1st Brillouin zone. The blue-shift of the G mode originates from a coupling of the optical
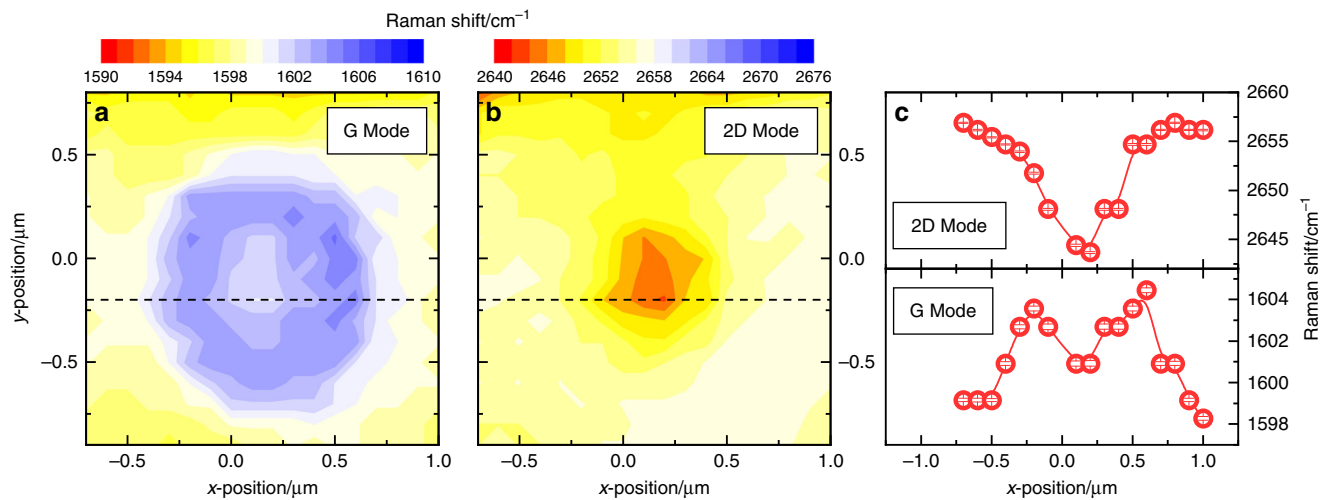
Fig. 2 Mode frequency in the vicinity of a gold nanoparticle. **a** and **b** maps of the Raman shifts of the G and 2D Raman modes close to a spherical gold nanoparticle, respectively. The laser wavelength of 633 nm is in-resonance with the localized surface-plasmon absorption of the gold nanoparticle. The maps correspond to the intensity maps shown previously. The G mode exhibits a blue-shift, whereas the 2D mode exhibits a red-shift when approaching the gold nanoparticle position. **c** The profiles of the position-dependent Raman shift along the dashed lines of the two maps are depicted on the right. The size of the error bars corresponds to the standard error of the Lorentzian fit function applied to the corresponding Raman line. Note that the error bars are smaller than the symbol size
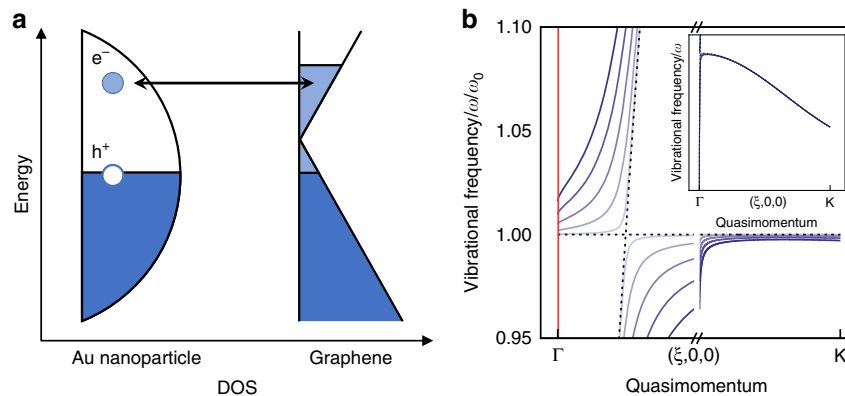

Fig. 3 Correlation between carrier concentration and hybridization strength. **a** Schematic illustration of hot-electron injection leading to the occupation of graphene's electronic states around the gold nanoparticle. The dark-shaded areas correspond to the electron distribution in equilibrium, while the area in lighter blue represents the additional electrons transferred after resonant illumination of the gold nanoparticle. **b** Qualitative behavior of the dispersions of the plasmon-phonon hybrid modes for various coupling strengths, i.e., different carrier concentrations, within the 1st Brillouin zone. The plasmon-phonon dispersions are normalized to the unperturbed phonon dispersion. A two-band anti-crossing model was assumed. The red line represents the photon dispersion relation, which indicates that the Raman G mode as a one-phonon Raman process is strongly affected by the level anti-crossing. The q-axis is divided into two regions where the linear scales differ by a factor of 75, i.e., the interval at low $|q|$ is magnified. The inset shows the same plasmon-phonon hybrid dispersions without normalization and on a linear scale on the entire q-axis between Γ and K. The dashed lines represent the uncoupled plasmon modes and phonon modes, respectively, while the blue solid lines represent the hybrid modes with increasing strength of coupling

phonon modes to light-induced free-carrier excitations, i.e., the surface-plasmon polariton (SPP) of graphene as predicted by Jablan et al.[30]. The transfer of hot-electrons from the resonantly excited gold nanoparticle provides free carriers invoking this plasmon–phonon coupling (see Fig. 3). Graphene's SPP branch behaves photon-like near the Γ-point with an energy dispersion relation $\omega \propto \sqrt{|q|}$, that is, proportional to the square root of the wave vector's absolute value[39]. The level anti-crossing between this free-carrier excitation and the optical phonons leads to the formation of two hybrid plasmon-phonon modes repelling each other at the intersection of the non-interacting SPP and phonon dispersions in reciprocal space. The strength of the level-repulsion scales with the free-carrier density. The upper branch possesses a phonon-like character at small wave vectors q, which

transforms into a SPP-like character with increasing q. The lower branch shows the opposite behavior, in other words, it is phonon-like close to the edges of the Brillouin zone at the K or the K' points. In the following, we will refer to the coupling between graphene's SPP and its optical phonons simply as plasmon–phonon coupling. The qualitative behavior of the plasmon–phonon coupling for different carrier densities is shown in Fig. 3a. The point of intersection occurs at small wave vectors q, i.e., close to the Γ-point, as the pristine SPP dispersion relation is quite steep. Thus, the coupling mainly affects the G mode at the Γ-point. In contrast, the dispersion close to the K and the K' points remains almost unaffected, which means, the effect of coupling on the frequency of the 2D mode is also weak. The relative frequency shift of the G mode close to the nanoparticle is,
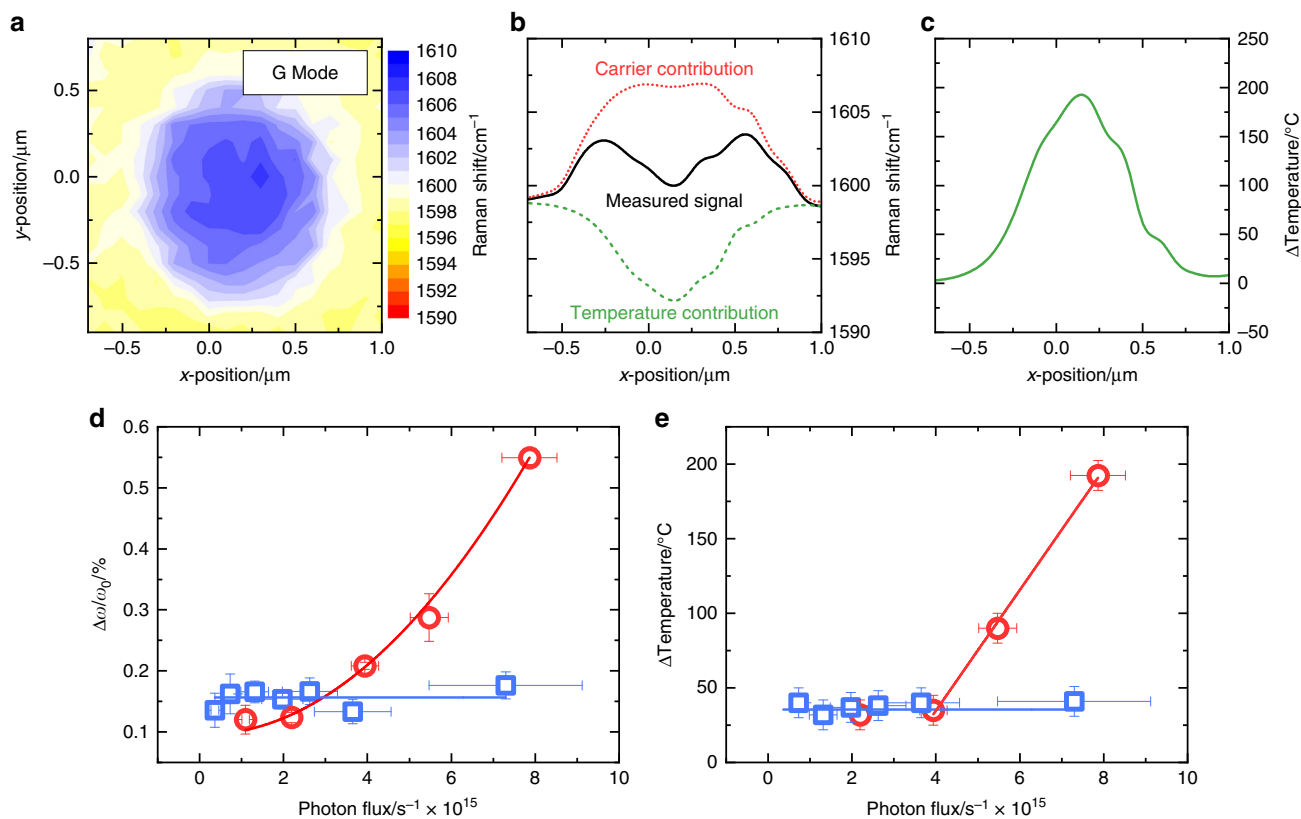
Fig. 4 Separating contributions due to heating and plasmon–phonon coupling and dependence on photon flux. **a** Map of the Raman shift of the G mode corrected for the temperature-induced red-shift. **b** Raman shift profile along the line through the center position of the nanoparticle divided into its temperature and plasmon–phonon-coupling distributions. **c** Temperature profile along the line deduced from the red-shift of the 2D mode. **d** Plasmon–phonon coupling induced blue-shift as a function of photon density of the 633 nm excitation laser for a pristine gold nanoparticle (red circles) and a silica-shelled gold nanoparticle (blue squares), respectively. **e** Local heating effect deduced from the red-shift of the 2D mode as a function of photon density of the 633 nm excitation laser for a pristine gold nanoparticle (red circles) and a silica-shelled gold nanoparticle (blue squares), respectively. The error bars along the abscissa shown in **d** and **e** correspond to an assumed uncertainty of the incident photon flux of 5% and those along the ordinate to the standard error of the two-dimensional Gaussian fit function used to model the maps of both, the temperature and plasmon–phonon coupling induced blue-shift of the G mode

therefore, strongly dependent on the change of the free-carrier concentration due to hot-electron injection.

Model calculations of the hybrid plasmon-phonon modes based on a simple level-repulsion model employing different coupling strengths, i.e., different hot-carrier densities, help to interpret the experimental results (see Fig. 3b). The modeling indicates that the G mode close to Γ is strongly affected by the level-repulsion, while the main contribution to the red-shift of the 2D mode is not related to plasmon–phonon coupling, but should rather be of a different origin. This assumption is supported by the findings of Das et al.[40], who showed that n-type doping has barely an influence on the frequency of the 2D mode as long as heavy doping is avoided.

Separating heating and plasmon–phonon coupling contributions. Raman modes of graphene show a red-shift with increasing temperature[41]. Thermalization of the LSPs of the gold nanoparticle after resonant excitation leads to a local heating of the nanoparticle itself and of the surrounding graphene. The high thermal conductivity of single-layer graphene of about 5000 W m^{-1} K^{-1} leads to an efficient dissipation of the heat in the graphene layer itself[5]. Thus, the spatial area where the Raman shifts are affected by additional heating is confined to the thermal contact between gold nanoparticle and graphene where the temperature gradient occurs. Nevertheless, the local temperature change affects the entire phonon dispersion relation across the whole Brillouin zone.

As the 2D mode is hardly affected by plasmon–phonon coupling, the local red-shift of the 2D mode may be entirely attributed to this local heating. In contrast, the mode position of the G mode is governed by the interplay of two effects: thermal effects leading to a red-shift and plasmon–phonon coupling leading to a blue-shift. Their interplay causes the crater-like appearance of the Raman shift profile of the G mode in the vicinity of the gold nanoparticle. The knowledge of the temperature-dependent Raman shifts of graphene's Raman modes in the range between 20 and 500 °C allows us to separate the temperature-induced red-shift from the blue-shift due to the hot-electron injection. The rates of the temperature shifts of the G and 2D mode determined by us are -0.035 cm^{-1} K^{-1} and -0.07 cm^{-1} K^{-1}, respectively, in accordance with values found in literature[41].

The temperature-induced red-shift of the G mode can be deduced using the two rates determined experimentally assuming that the red-shift of the 2D mode is entirely temperature-induced. Thus, the spatial map of the Raman shift of the G mode shown in Fig. 2a may be corrected for temperature effects accordingly. One obtains a distribution corresponding to a single peak centered at the position of the gold nanoparticle as shown in Fig. 4a. The position-dependent Raman shift of the G mode along a line through the center of the gold nanoparticle can, thus, be divided into a temperature-induced part and a plasmon–phonon coupling induced part. Both are plotted in Fig. 4b together with the original M-shaped profile. The plasmon–phonon coupling induced

contribution of the profile becomes a broad single peak after correction. This is expected for free carriers localized at the interface between the nanoparticle and graphene. The temperature variation appears somewhat narrower due to the local heating; the extracted temperature profile is shown in Fig. 4c. It should be noted that the temperature profile is not a steady state temperature distribution occurring with the laser located at a fixed position. As the laser is scanned along the line, the temperature value at each position of the profile corresponds to an average temperature arising in the steady-state situation when the laser is focused onto this particular position. The same holds for the profile of the plasmon–phonon coupling induced contribution, i.e. it does not reflect a steady-state spatial carrier profile.

The local heating shown in Fig. 4c reveals a temperature rise by almost 200 °C at the position of the gold nanoparticle. This surprisingly large effect may be due to either direct heating of the graphene by strong light absorption enhanced by the antenna action of the gold nanoparticle or due to heat and hot-electrons generated by the light absorption within the gold nanoparticle and then transferred to the graphene layer. Studying the local heating in the vicinity of a nanoparticle as a function of photon flux of the excitation laser using the red-shift of the 2D mode as temperature probe yields further insight, when performing this experiment for a pristine gold nanoparticle and a silica-shelled gold nanoparticle. In case of the former, in particular, the hot-electron transfer to the graphene is possible, in case of the latter, it is hindered or even impeded by the electronic barrier imposed by the silica shell of the nanoparticle. The same somewhat holds for the heat transfer from the gold nanoparticle to graphene. The results of the flux dependent analysis (Fig. 4d, e) reveal clear differences for the pristine gold nanoparticle and the gold nanoparticle with silica shell. The plasmon–phonon coupling induced blue-shift of the G mode and the deduced local heating increase dramatically with increasing photon flux in case of the pristine gold nanoparticle whereas they are almost independent of photon flux in case of the silica-shelled nanoparticle.

In order to rule out, differences in terms of the antenna action, we performed finite-element simulations of the electric-field enhancement close to the surface of the two types of nanoparticles using the *RF* module of *Comsol*. The electric-field enhancement close to the particles' surfaces to first-order approximates their expected LSP response. The resulting resonance curves are depicted in Fig. 5a. Both curves exhibit similar behavior with an almost equal resonance frequency. As the LSP absorption of the two nanoparticles is very similar (see Fig. 5a), the heat deposited by LSP absorption of the nanoparticle inside the nanoparticle should be comparable. Thus, the strong local heating in case of the pristine gold nanoparticle is related to heat and hot-electron-transfer from the particle to the graphene layer and not to direct heating of the graphene layer enhanced by the antenna action of the gold nanoparticle. The transfer process can be considered a stationary state under continuous-wave laser-excitation, which increases the electron concentration in the graphene around the gold nanoparticle. Furthermore, the excess energy of these hot-electrons is transferred to the graphene lattice and contributes to the significant local heating. Both effects are impeded in case of the silica-shelled nanoparticle.

Comparison of in- and off-resonance measurements. A third contribution to the Raman shift may be due to strain. The influence of strain on the phonon modes may be accounted for similar to that of temperature, that is, by taking into account the known shift rates of the Raman mode frequencies with strain[42]. The G mode as well as the 2D mode exhibit a red-shift under tensile
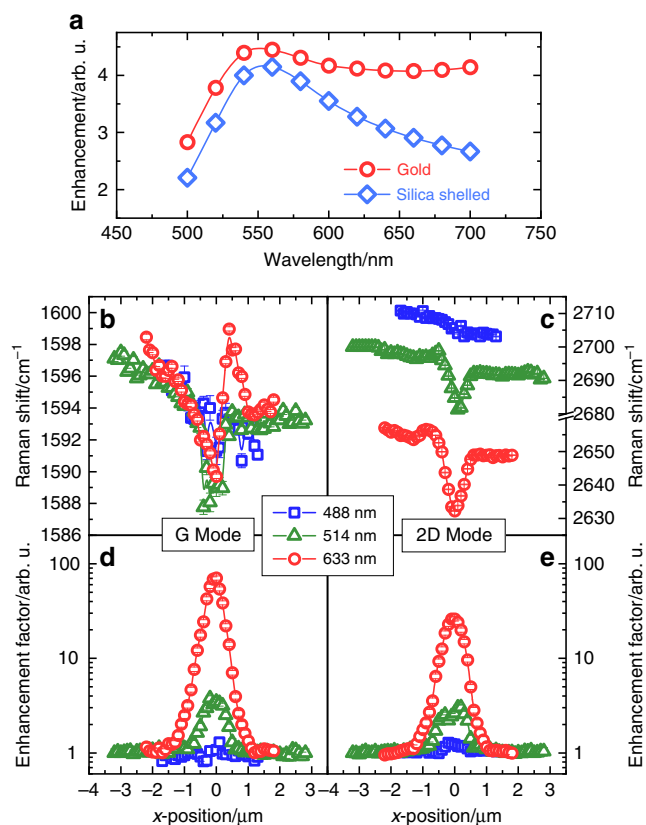
Fig. 5 Wavelength dependence of the effects observed. **a** *Comsol* calculations of the electric-field enhancement at the gold surface for pristine gold and silica-shelled gold nanoparticles with lateral dimensions corresponding to the manufacturers' specifications. Linear spatial profiles of the Raman shift (**b**, **c**) and the enhancement factor (**d**, **e**) of the Raman G and 2D modes for three different excitation wavelengths, i.e., 633 nm (red circles), 514 nm (green triangles) both in-resonance with the localized surface-plasmon absorption of the gold nanoparticle, and 488 nm (blue squares) off-resonance. In case of the Raman shift profiles (**b**, **c**) the error bars correspond to the standard error of the Lorentzian fit used to model the spectra. In case of the Enhancement factor profiles (**d**, **e**) the error bars correspond to the maximal error composed of the intensity deviation of the unenhanced areas and the standard error of the Lorentzian fit used

uniaxial strain. The G mode even splits into a G$^+$ and a G$^-$ mode for uniaxial strains larger than 0.5%. However, at lower strains, the rates of the strain-induced shifts of G and 2D mode are −21.2 cm^{-1}/% and −64 cm^{-1}/%, respectively. These rates are to a first approximation independent of the excitation laser wavelength. A complication arises as the Raman shift of the 2D mode, in contrast to that of the G mode, is strongly dependent on the wavelength of the exciting laser due to the peculiarities of the underlying double-resonance process[43]. Nevertheless, varying the excitation photon energy allows one to distinguish between strain and temperature effects. Heating should only be observed for red and green excitation at 633 and 514 nm, respectively, but not for excitation in the blue, i.e., at 488 nm wavelength according to the LSP response of the gold nanoparticle in Fig. 5a.

Raman mappings of another gold nanoparticle on graphene obtained at different excitation energies and comparable laser powers corroborate these interpretations. Figure 5 shows the spatial profiles obtained for the Raman shift (a, b) and the enhancement factors (c, d) of the graphene G and 2D modes. All profiles are recorded along the same line passing through the center position of this particular gold nanoparticle. The
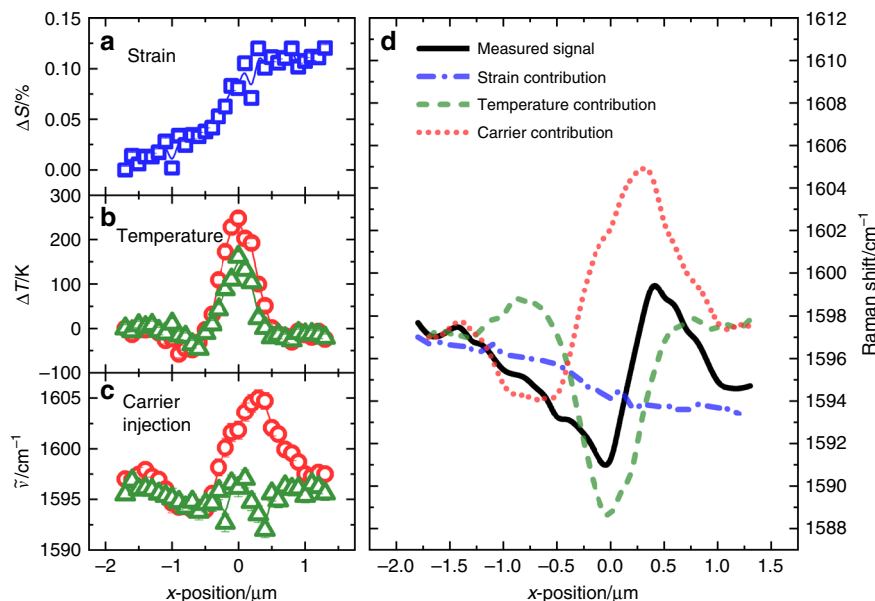
Fig. 6 Separation of the contributions due to strain, temperature, and carrier injection. **a** Calculated relative strain profile based on the Raman shift profile of the 2D mode measured with off-resonance excitation of 488 nm, where the data point at $x = -1.7\,\mu m$ defines zero as a reference. The error bars correspond to the standard deviation of the Lorentzian fit function used to model the Raman modes. **b** Calculated relative temperature profiles based on the strain-corrected Raman shift profiles of the 2D mode measured with an excitation wavelength of 514 nm and 633 nm, again the data point at $x = -1.7\,\mu m$ defines zero as a reference. **c** Raman shift profiles of the G mode corrected for strain and temperature contributions, which, thus, is exclusively caused by the injected hot-electrons. The error bars shown in **b** and **c** correspond to the maximal error obtained by means of error propagation, respectively. **d** Comparison of magnitudes of the three contributions due to strain, temperature, and hot-carriers to the Raman shift profile of the G mode at 633 nm excitation

enhancement effects are strongest for the excitation wavelength of 633 nm, already considerably weaker for 514 nm, and almost vanishing for 488 nm excitation. This observation is in agreement with the calculations of the LSP-induced field enhancement shown in Fig. 5a.

Finally, the true plasmon–phonon coupling induced effects are isolated after the effects of strain and temperature in graphene due to the nanoparticle's presence have been identified. Clearly, the Raman shift profiles obtained (Fig. 5b, c) somewhat deviate from those shown in Fig. 1 for the first gold nanoparticle studied as the absolute influence on the Raman shift due to plasmon–phonon coupling, strain, and temperature will vary from sample to sample. In this particular case, the linearly decreasing background of the Raman shift profiles is solely due to a strain gradient within the graphene layer since the profile of the 2D mode measured with an excitation wavelength of 488 nm (see Fig. 5c) does not show specific features related to the gold nanoparticle. The LSP absorption of the gold nanoparticle at 488 nm is off-resonance and, hence, small. Local heating and hot-carrier effects are negligible and the Raman shift profiles of G and 2D mode at 488 nm solely reflect the variation of strain in the graphene. As the effect of strain on the G mode frequency is independent of excitation laser wavelength, the strain contribution can be quantified by analysis of the G mode Raman shift profile by using the coefficients for tensely strained graphene from the literature[42] and be eliminated from the corresponding profiles obtained at 633 and 514 nm. The spatial variation of strain is quantified in Fig. 6a. The resulting Raman shift profiles corrected for strain may then be used to derive the spatial temperature profiles for 633 and 514 nm excitation shown in Fig. 6b. This is done assuming that the frequency of the 2D mode is basically unaffected by plasmon–phonon coupling. These profiles, in turn, permit a temperature correction of the Raman shift profiles of the G mode. Thus, the solely plasmon–phonon

coupling induced contribution of the Raman shift profiles of the G mode at the two excitation wavelengths can be derived and is depicted in Fig. 6c. The strain and temperature corrected profiles of the Raman shift of the G mode reveal that a significant plasmon–phonon coupling induced contribution due to hot-electron injection from the gold nanoparticle to the graphene, is only present in case of 633 nm excitation, in other words, in case of in-resonance excitation. Figure 6d visualizes all three absolute contributions to the full Raman shift profile of the G mode for 633 nm. The curves displayed emphasize that the frequency shift of the Raman G mode due to the change in free-carrier concentration is on the same scale as the temperature-induced red-shift for resonant LSP excitation of the gold nanoparticle. The local heating effects are comparable to those of the other pristine gold nanoparticle at 633 nm wavelength excitation.

Verification of the analysis method presented. In order to further validate our findings and the analysis procedure, in particular, we applied the method introduced by Lee et al. for analyzing the Raman signals of graphene. The presentation of the data in a ω_{2D} versus ω_G plot where ω_{2D} and ω_G denote the peak positions of the G and 2D Raman signals allows one to distinguish regions of the sample affected either by strain or additional charge doping[30]. The method was exemplarily applied to the Raman data depicted in Fig. 2 because for that particular mapping the regions affected by strain, charge transfer, and temperature are well separated. The corresponding ω_{2D} vs. ω_G plot is shown in Fig. 7a. Below, we depict the corresponding map of the G mode position (Fig. 7b) and maps of three groups of data points denoting regions of the sample, which exhibit different dominant effects. Group I (see Fig. 7c) corresponds to positions on the graphene, which are not affected by the Au nanoparticle, the differences in the corresponding spectra arise mainly due to local strain effects. The data points in Fig. 7a corresponding to group I
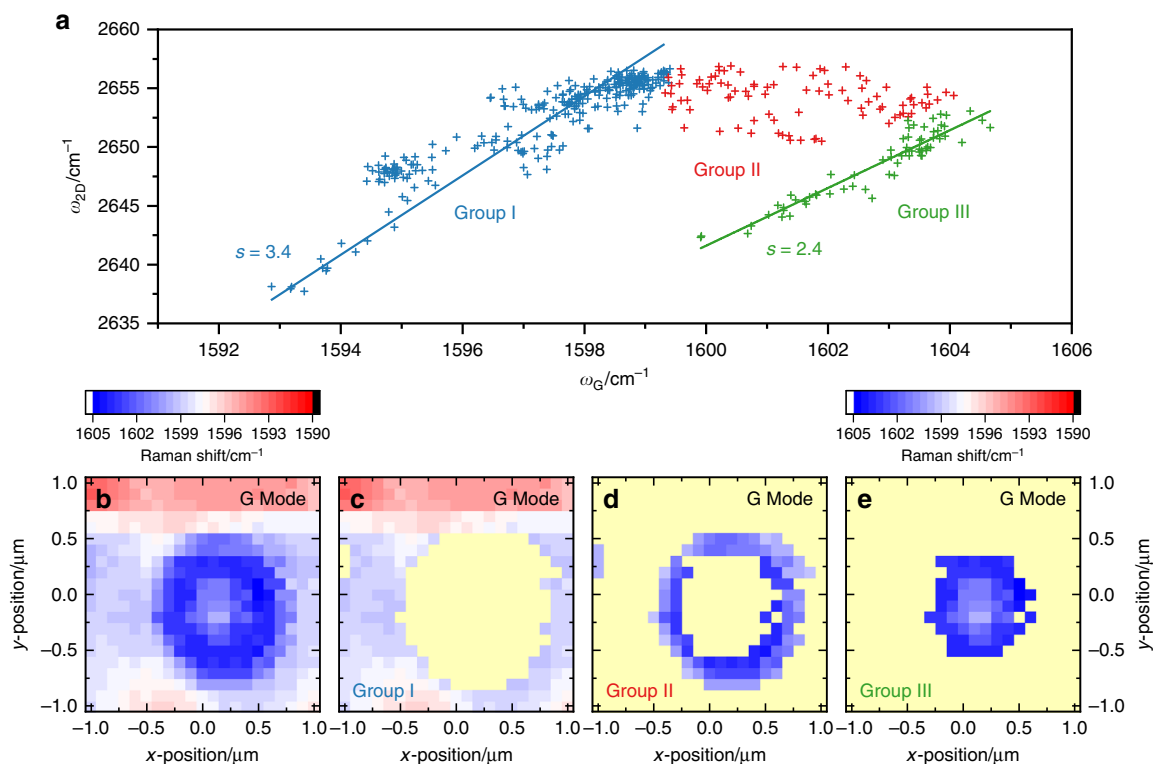
Fig. 7 Verification of the analysis method presented by plotting the data in a ω_{2D} vs. ω_G plot. **a** Separation of spatial regions dominated by strain (**c**), hot-carrier transfer (**d**), and temperature effects (**e**) in the G and 2D mappings as described in the text and shown in **b** according to the analysis method introduced by Lee et al.[44]. The slopes of the blue and green line are indicative for dominant mechanical strain and to dominating temperature effects, respectively. **b** Spatial mapping of the Raman G mode frequency. **c** Spatial mapping of the Raman G mode frequency including only the data points of (**a**), that are related to mechanical strain, i.e., group I. **d** Spatial mapping of the Raman G mode frequency including only the data points of **a** that are related to hot-carrier transfer, i.e., group II. **e** Spatial mapping of the Raman G mode frequency including only the data points of **a**, that are related to a high and nearly constant carrier concentration with an additional temperature contribution, i.e., group III. Spatial areas those data points are not included in the definition of groups I, II, and III are plotted in yellow in **c**, **d**, and **e**, respectively

are shown in blue. They are well fitted by a straight line with a slope of $(\Delta\omega_{2D}/\Delta\omega_G)\varepsilon = 3.4$. This is in good agreement with the value found by Mohiuddin et al.[42] when an average value for $\partial\omega_G^+/\partial\varepsilon$ and $\partial\omega_G^-/\partial\varepsilon$ is used. The sample positions assigned to group II form a circle around the nanoparticle in Fig. 7d. In this region, the graphene Raman spectra are modified by the hot-carrier injection according to the analysis in Fig. 4. The corresponding data points form a virtually horizontal line in Fig. 7a. The Raman spectra in the region of the sample below and close to the nanoparticle (Fig. 7e) are dominated by temperature changes in addition to hot-carrier injection. The corresponding data points shown in green form the line like arrangement on the right hand side of Fig. 7a. Here, a lesser slope of $(\Delta\omega_{2D}/\Delta\omega_G)\varepsilon = 2.4$ well describes the data. Thus, Raman mappings as proposed by us, indeed, yield valuable information about the interaction of an individual Au nanoparticle with the underlying graphene layer.

Discussion
In conclusion, spectroscopic spatial Raman mappings are a powerful noninvasive probe for studying the interactions of plasmonic nanoparticles with their environment under photon irradiation. The behavior of the Raman modes related to graphene phonons in the vicinity of single gold nanoparticles differ significantly depending on the excitation, i.e., whether it is in-resonance with their nanoparticle's LSPs (633 nm) or off-resonance (488 nm). In resonance, the G mode of the surrounding graphene exhibits a blue-shift whereas the 2D mode

shows a clear red-shift. The gold nanoparticle significantly enhances all Raman modes, the G mode, the D mode, and the 2D mode with the enhancement of the D mode being much larger than those of the G mode and the 2D mode. For off-resonance excitation, the presence of the gold nanoparticle has little impact on the phonons of the surrounding graphene, almost no enhancement and no shift of the Raman modes are observed, which can be correlated with the presence of the nanoparticle. The off-resonance behavior of the Raman profiles can be fully explained by strain effects. The in-resonance behavior can be accounted for by additionally assuming local thermal heating and a coupling between the graphene phonons at the Γ-point and collective excitations of hot-carriers transferred from the gold nanoparticle after LSP excitation. A careful comparison of the in-resonance and the off-resonance data allows us to separate the three contributions: plasmon–phonon coupling, heating, and strain effects. Control experiments on gold nanoparticles with silica shells prohibiting the hot-electron transfer to the graphene fully corroborate our explanation.

Systematic performance of such experiments employing different combinations of 2D materials and metal nanoparticles in conjunction with theory will allow us to obtain a fundamental understanding of the plasmonic interaction of metal nanoparticles with their environment. Thereby, insights are provided into physical processes at nanoscale contacts on graphene devices as well as references for future photonic devices based on the combination of plasmonic structures and 2D materials in general.

Methods

Sample preparation. The samples studied were prepared using commercially available graphene (*Graphenea Inc.*) grown by chemical vapor deposition (CVD) on copper foil. The graphene has been transferred onto a $1 \times 1\ cm^2$ quartz substrate with a thickness of 0.5 mm according to the recipe given by the vendor. Hall measurements yielded a weak p-type behavior of the graphene sheets on quartz.

The gold (*BBI Solutions OEM Ltd.*) and silica-shelled gold nanoparticles (*nanoComposix, Inc.*) are also commercially available. The gold nanoparticles have an average diameter of 250 nm, are suspended in aqueous solution containing 0.01 % choloauric acid ($HAuCl_4$), and are citrate stabilized. The silica-shelled gold nanoparticles have an average core diameter of 100 nm while the silica shell has thickness of 20 nm. These particles are suspended in ethanol. Both suspensions have been highly diluted to a concentration of approx. 5×10^5 ppml and have been deposited onto the particular graphene-quartz substrate, yielding isolated gold resp. silica-shelled gold nanoparticles after drying.

Experimental details. The Raman mappings were performed in back scattering geometry with a set-up consisting of a *Leica* top-illuminating bright-field microscope with a *Leica* 50 × /0.75 NA objective and a *Renishaw InVia* spectrometer equipped with a charge-coupled device camera providing a spectral resolution of $1.5\ cm^{-1}$. The maximum applied laser powers did not exceed 5 mW in all experiments. The lateral resolution is limited to a step size of 100 nm. In all maps, *x* indicates the fast and *y* the slow scanning direction, while a unidirectional scan mode was applied. A temperature controllable stage by *Linkam Scientific Instruments* in combination with an *Olympus* 50×/0.45 NA objective has been used for the temperature-dependent Raman measurements. The Hall measurements have been performed at 280 K using an Oxford superconducting magnet system providing magnetic fields between −10 and 10 T.

Data evaluation. The Raman spectra collected are corrected for background signals. A function composed of four Lorentzians each multiplied by a factor are used to fit the background-corrected spectra. Three of the four Lorentzians are used to model the three investigated Raman modes, while the fourth accounts for a weak signal between 2400 and 2500 cm^{-1} that is often referred-to as the G* mode (see Fig. 1a)[43]. Thus, an impact of the G* signal on the analysis of the 2D mode is prevented. A two-dimensional Gaussian function is used to model the corresponding Raman shift maps in order to perform the quantitative analysis of the relative G mode shifting in dependence on the incident photon flux.

Data availability

The data that support the findings of this study are available from the authors on reasonable request.

References

1. Novoselov, K. S. et al. Electric field in atomically thin carbon films. *Science* **306**, 666–669 (2004).
2. Chen, J. H., Jang, C., Xiao, S., Ishigami, M. & Fuhrer, M. S. Intrinsic and extrinsic performance limits of graphene devices on SiO2. *Nat. Nanotechnol.* **3**, 206–209 (2008).
3. Lee, C., Wei, X., Kysar, J. W. & Hone, J. Measurement of the elastic properties and intrinsic strength of monolayer graphene. *Science* **321**, 385–388 (2008).
4. Castro Neto, A. H., Guinea, F., Peres, N. M. R., Novoselov, K. S. & Geim, A. K. The electronic properties of graphene. *Rev. Mod. Phys.* **81**, 109–162 (2009).
5. Balandin, A. A. et al. Superior thermal conductivity of single-layer graphene. *Nano Lett.* **8**, 902–907 (2008).
6. Politano, A. & Chiarello, G. Probing the Young's modulus and Poisson's ratio in graphene/metal interfaces and graphite: a comparative study. *Nano Res.* **8**, 1847–1856 (2015).
7. Bonaccorso, F., Sun, Z., Hasan, T. & Ferrari, A. C. Graphene photonics and optoelectronics. *Nat. Photonics* **4**, 611–622 (2010).
8. Shahil, K. M. F. & Balandin, A. A. Thermal properties of graphene and multilayer graphene: Applications in thermal interface materials. *Solid State Commun.* **152**, 1331–1340 (2012).
9. Liu, Y., Dong, X. & Chen, P. Biological and chemical sensors based on graphene materials. *Chem. Soc. Rev.* **41**, 2283–2307 (2012).
10. Liu, M., Zhang, R. & Chen, W. Graphene-supported nanoelectrocatalysts for fuel cells: Synthesis, properties, and applications. *Chem. Rev.* **114**, 5117–5160 (2014).
11. Gugliuzza, A., Politano, A. & Drioli, E. The advent of graphene and other two-dimensional materials in membrane science and technology. *Curr. Opin. Chem. Eng.* **16**, 78–85 (2017).
12. Bao, Q. & Loh, K. P. Graphene photonics, plasmonics, and broadband optoelectronic devices. *ACS Nano* **6**, 3677–3694 (2012).
13. Nair, R. R. et al. Fine structure constant defines visual transparency of graphene. *Science* **320**, 1308 (2008).
14. Kreibig, U. & Vollmer, M. *Optical Properties of Metal Clusters.* (Springer, Berlin Heidelberg, 1995).
15. Raether, H. *Surface Plasmons on Smooth and Rough Surfaces and on Gratings.* (Springer, Berlin Heidelberg, 1988).
16. Willets, K. A. & Van Duyne, R. P. Localized surface plasmon resonance spectroscopy and sensing. *Annu. Rev. Phys. Chem.* **58**, 267–297 (2007).
17. Landau, L. D. On the vibrations of the electronic plasma. *J. Phys.* **10**, 25–34 (1946).
18. Lee, J., Mubeen, S., Ji, X., Stucky, G. D. & Moskovits, M. Plasmonic photoanodes for solar water splitting with visible light. *Nano Lett.* **12**, 5014–5019 (2012).
19. Mukherjee, S. et al. Hot electrons do the impossible: Plasmon-induced dissociation of H2on Au. *Nano Lett.* **13**, 240–247 (2013).
20. Politano, A. et al. Photothermal membrane distillation for seawater desalination. *Adv. Mater.* **29**, 1603504 (2017).
21. Politano, A. et al. When plasmonics meets membrane technology. *J. Phys. Condens. Matter* **28**, 363003 (2016).
22. Fang, Z. et al. Graphene-antenna sandwich photodetector. *Nano Lett.* **12**, 3808–3813 (2012).
23. Fang, Z. et al. Plasmon-induced doping of graphene. *ACS Nano* **6**, 10222–10228 (2012).
24. Amendola, V., Pilot, R., Frasconi, M., Maragò, O. M. & Iati, M. A. Surface plasmon resonance in gold nanoparticles: a review. *J. Phys. Condens. Matter* **29**, 203002 (2017).
25. Eustis, S. & El-Sayed, M. A. Why gold nanoparticles are more precious than pretty gold: Noble metal surface plasmon resonance and its enhancement of the radiative and nonradiative properties of nanocrystals of different shapes. *Chem. Soc. Rev.* **35**, 209–217 (2006).
26. Jain, P. K. & El-Sayed, M. A. Plasmonic coupling in noble metal nanostructures. *Chem. Phys. Lett.* **487**, 153–164 (2010).
27. Michaelson, H. B. The work function of the elements and its periodicity. *J. Appl. Phys.* **48**, 4729–4733 (1977).
28. Giovannetti, G. et al. Doping graphene with metal contacts. *Phys. Rev. Lett.* **101**, 026803 (2008).
29. Manjavacas, A., Liu, J. G., Kulkarni, V. & Nordlander, P. Plasmon-induced hot carriers in metallic nanoparticles. *ACS Nano* **8**, 7630–7638 (2014).
30. Jablan, M., Soljačić, M. & Buljan, H. Unconventional plasmon-phonon coupling in graphene. *Phys. Rev. B* **83**, 161409 (2011).
31. Lazzeri, M. & Mauri, F. Nonadiabatic Kohn anomaly in a doped graphene monolayer. *Phys. Rev. Lett.* **97**, 266407 (2006).
32. Tse, W. K., Hu, B. Y. K. & Das Sarma, S. Chirality-induced dynamic kohn anomalies in graphene. *Phys. Rev. Lett.* **101**, 066401 (2008).
33. Yan, J., Zhang, Y., Kim, P. & Pinczuk, A. Electric field effect tuning of electron-phonon coupling in graphene. *Phys. Rev. Lett.* **98**, 166802 (2007).
34. Politano, A., Formoso, V. & Chiarello, G. Evidence of composite plasmon-phonon modes in the electronic response of epitaxial graphene. *J. Phys. Condens. Matter* **25**, 345303 (2013).
35. Politano, A., De Juan, F., Chiarello, G. & Fertig, H. A. Emergence of an out-of-plane optical phonon (ZO) kohn anomaly in quasifreestanding epitaxial graphene. *Phys. Rev. Lett.* **115**, 075504 (2015).
36. Dresselhaus, M. S., Dresselhaus, G. & Jorio, A. *Group Theory Application to the Physics of Condensed Matter.* (Springer, Berlin Heidelberg, 2008).
37. Pimenta, M. A. et al. Studying disorder in graphite-based systems by Raman spectroscopy. *Phys. Chem. Chem. Phys.* **9**, 1276–1290 (2007).
38. Ferrari, A. C. & Basko, D. M. Raman spectroscopy as a versatile tool for studying the properties of graphene. *Nat. Nanotechnol.* **8**, 235–246 (2013).
39. Hwang, E. H. & Das Sarma, S. Dielectric function, screening, and plasmons in two-dimensional graphene. *Phys. Rev. B* **75**, 205418 (2007).
40. Das, A. et al. Monitoring dopants by Raman scattering in an electrochemically top-gated graphene transistor. *Nat. Nanotechnol.* **3**, 210–215 (2008).
41. Calizo, I. et al. Raman nanometrology of graphene: Temperature and substrate effects. *Solid State Commun.* **149**, 1132–1135 (2009).
42. Mohiuddin, T. M. G. et al. Uniaxial strain in graphene by Raman spectroscopy: G peak splitting, Grüneisen parameters, and sample orientation. *Phys. Rev. B* **79**, 1–8 (2009).
43. Malard, L. M., Pimenta, M. A., Dresselhaus, G. & Dresselhaus, M. S. Raman spectroscopy in graphene. *Phys. Rep.* **473**, 51–87 (2009).
44. Lee, J. E., Ahn, G., Shim, J., Lee, Y. S. & Ryu, S. Optical separation of mechanical strain from charge doping in graphene. *Nat. Commun.* **3**, 1024–1028 (2012).

Author contributions

M.W. performed the experiments. M.W., S.C., and P.J.K. discussed the data, co-wrote the manuscript and have given approval to the final version of the manuscript.

Additional information

Competing interests: The authors declare no competing interests.

Reprints and permission information is available online at http://npg.nature.com/reprintsandpermissions/

Publisher's note: Springer Nature remains neutral with regard to jurisdictional claims in published maps and institutional affiliations.